NSRRC-Jo 5/155 (2016)

Energy & Environmental Science

PAPER

View Article Online
View Journal | View Issue

Published on 11 January 2016. Downloaded by National Chiao Tung University on 30/05/2016 03:34:40.

Cite this: *Energy Environ. Sci.*, 2016, 9, 1282

Intermixing-seeded growth for high-performance planar heterojunction perovskite solar cells assisted by precursor-capped nanoparticles†

Shao-Sian Li,[a] Chi-Huang Chang,[b] Ying-Chiao Wang,[a] Chung-Wei Lin,[a] Di-Yan Wang,[c] Jou-Chun Lin,[c] Chia-Chun Chen,[cd] Hwo-Shuenn Sheu,[e] Hao-Chung Chia,[f] Wei-Ru Wu,[e] U-Ser Jeng,*[ef] Chi-Te Liang,[b] Raman Sankar,[gh] Fang-Cheng Chou[gh] and Chun-Wei Chen*[ah]

Received 21st October 2015,
Accepted 7th January 2016

DOI: 10.1039/c5ee03229f

www.rsc.org/ees

This work proposes a novel approach to modulate the nucleation and growth of perovskite crystals in planar perovskite ($CH_3NH_3PbI_{3-x}Cl_x$) solar cells by intermixing precursor-capped inorganic nanoparticles of PbS. A small amount of dispersed PbS nanoparticles which were covered with perovskite precursor molecules of methylammonium iodide (CH_3NH_3I, MAI) through the ligand-exchange treatment functioned as effective seed-like nucleation sites to promote the formation of perovskite lattice structures. Through this intermixing-seeded growth technique, substantial morphological improvements, such as increased crystal domains, enhanced coverage, and uniformity, were realized in the perovskite thin films, and the corresponding solar cell devices exhibited a promising power conversion efficiency of 17.4%, showing an enhancement of approximately 25% compared to that of the controlled pristine solar cell device. The substantially enhanced crystal orientation, particularly along the direction perpendicular to the substrate, was evident from the synchrotron-based grazing incidence wide-angle X-ray scattering data. This observation was consistent with the enhanced carrier diffusion lengths and excellent reproducibility of high fill factors of the planar heterojunction perovskite devices fabricated through the proposed technique.

Broader context

It is known that morphology and crystallization of perovskite thin films are sensitive to the nucleation and growth kinetics, which strongly depend on the energy barrier of the reaction. This work demonstrates a novel approach to modulate the nucleation and growth of perovskite crystals in planar perovskite ($CH_3NH_3PbI_{3-x}Cl_x$) solar cells by intermixing a small amount of precursor-capped inorganic PbS nanoparticles during film growth. Through the interfacial engineering of PbS nanoparticles, methylammonium iodide molecules (CH_3NH_3I, MAI) which is one of the precursors of $CH_3NH_3PbI_{3-x}Cl_x$, were intentionally pre-capped on the surface of PbS nanoparticles. The dispersed MAI-modified PbS nanoparticles functioned as effective seed-like sites to promote the formation of perovskite lattice structures, resulting in substantial morphological improvements. Perovskite solar cell devices fabricated through this intermixing-seeded growth technique exhibited a promising PCE of more than 17% with reproducible high fill factors (FFs) of the fabricated devices. Our results suggest that the intermixing-seeded growth technique by including a small amount of seed-like precursor-capped inorganic nanoparticles during film growth can effectively modulate the nucleation and growth of perovskite crystals, thus providing a new method to fabricate high-performance planar heterojunction perovskite-based solar cells.

[a] *Department of Materials Science and Engineering, National Taiwan University, No. 1, Sec. 4, Roosevelt Rd., Taipei, 10617, Taiwan. E-mail: chunwei@ntu.edu.tw*
[b] *Department of Physics, National Taiwan University, No. 1, Sec. 4, Roosevelt Rd., Taipei, 10617, Taiwan*
[c] *Department of Chemistry, National Taiwan Normal University, No. 88, Sec. 4, Ting-Chow Rd, Taipei, 11677, Taiwan*
[d] *Institute of Atomic and Molecular Sciences, Academia Sinica, No. 1, Sec. 4, Roosevelt Rd, Taipei, 10617, Taiwan*
[e] *National Synchrotron Radiation Research Center, No. 101, Hsin-An Road, Hsinchu, 30077, Taiwan. E-mail: usjeng@nsrrc.org.tw*
[f] *Chemical Engineering Department, National Tsing-Hua University, Hsinchu, 30013, Taiwan*
[g] *Center for Condensed Matter Sciences, National Taiwan University, No. 1, Sec. 4, Roosevelt Rd., Taipei, 10617, Taiwan*
[h] *Taiwan Consortium of Emergent Crystalline Materials (TCECM), Ministry of Science and Technology, No. 1, Sec. 4, Roosevelt Rd, Taipei, 10617, Taiwan*
† Electronic supplementary information (ESI) available: Details of materials synthesis, device fabrication and measurements. See DOI: 10.1039/c5ee03229f

This journal is © The Royal Society of Chemistry 2016

Published on 11 January 2016. Downloaded by National Chiao Tung University on 30/05/2016 03:34:40.

Introduction

The power conversion efficiencies (PCEs) of solar cells fabricated using organic–inorganic hybrid perovskite materials of $CH_3NH_3PbX_3$ (X = Cl, Br, or I) have progressed remarkably in the past few years because of the superior physical properties of perovskite materials, such as high optical absorption coefficients,[1–3] low binding energies of photo-excited electron–hole pairs,[2,4] and long and balanced electron–hole diffusion lengths.[5,6] The major challenge in this field lies in fabricating high-quality films using solution processes with controllable morphologies, high crystallinity, minimum pinhole formation, and high surface coverage to avoid low-resistance shunting paths.[7] It is known that the morphology and crystallization of perovskite thin films are sensitive to the nucleation and growth kinetics, which strongly depend on the energy barrier of the reaction. Heterogeneous nucleation is typically preferred over homogeneous nucleation during the crystal growth process, wherein the nucleation barrier is much lower at the liquid–solid interface than at areas away from this interface because of the wetting property imposed by the liquid–solid interface.[8] This phenomenon leads to easier nucleation of perovskite when the precursor solution is deposited on a substrate with a large surface area, such as the mesoporous metal oxide scaffold in mesoscopic perovskite solar cell devices, compared with a flat substrate.[7] Therefore, it becomes challenging yet critical at manipulating the growth kinetics to improve the morphology and crystallinity of perovskite solar cells consisting of a planar heterojunction device structure. For example, thermal annealing,[9–11] solvent engineering,[12–14] and incorporating a small amount of chemical additives[15–18] in the perovskite precursor solution which have been found to enhance the performance of solar cell devices by controlling the morphology, coverage, grain sizes, or the degree of crystallinity of perovskite films, have significant impact on PCEs of devices. In this work, we would like to propose a novel approach to modulate the nucleation and growth of perovskite crystals in planar perovskite ($CH_3NH_3PbI_{3-x}Cl_x$) solar cells by intermixing a small amount of precursor-capped inorganic PbS nanoparticles during film growth. Through the interfacial engineering of PbS nanoparticles, methylammonium iodide molecules (CH_3NH_3I, MAI) which is one of the precursors of $CH_3NH_3PbI_{3-x}Cl_x$, were intentionally pre-capped on the surface of PbS nanoparticles. The dispersed MAI-modified PbS nanoparticles functioned as effective seed-like sites to promote the formation of perovskite lattice structures, resulting in substantial morphological improvements. Perovskite solar cell devices fabricated through this intermixing-seeded growth technique exhibited a promising PCE of more than 17%, an enhancement of approximately 25% compared with that of the controlled pristine solar cell device. In particular, the high fill factors (FFs) of the fabricated devices were highly reproducible because of the substantially enhanced crystallinity of the perovskite films along the direction perpendicular to the substrate and hence an increased carrier diffusion length both of the electron and the hole. Our results suggested that the intermixing-seeded growth technique by including a small amount of seed-like precursor-capped inorganic nanoparticles during film growth can effectively modulate the nucleation and growth of perovskite crystals, thus providing a new method to fabricate high-performance planar heterojunction perovskite-based solar cells.

Results and discussion

Inorganic nanoparticles used in the present study were solution-phased PbS nanoparticles synthesized using lead(II) oxide (PbO) and bis(trimethylsilyl) sulfide, according to a modified Hines method.[19,20] Fig. 1(a) shows the transmission electron microscopy (TEM) image of the uniformly distributed PbS nanoparticles with a diameter of approximately 5 nm. The high resolution TEM (HRTEM) image (inset) revealed a *d*-spacing value of 0.342 nm corresponding to the (111) plane of the rock-salt structure of PbS. Prior to adding PbS nanoparticles in the perovskite precursor solution, several critical problems must be overcome. First, the surfaces of the as-synthesized PbS nanoparticles were capped with oleic acid (OA) which has a long alkyl chain and is often used in nanoparticle synthesis to control the dimension of nanoparticles and to prevent their aggregation. However, OA ligands largely limit the solubility of PbS nanoparticles in the dimethylformamide (DMF) solvent which was used to dissolve the $CH_3NH_3PbI_{3-x}Cl_x$ precursors. To improve the miscibility, ligand exchange treatment became essential. Using the concept of halide-based ligand-exchange treatment of colloidal quantum dots,[21–24] the originally capped OA ligands on the surface of PbS nanoparticles were replaced with halide molecules CH_3NH_3I (MAI) which is one of the precursors of $CH_3NH_3PbI_{3-x}Cl_x$ and is fully compatible with DMF solvent as shown in Fig. 1(b). The as-synthesized PbS nanoparticles capped with OA were dispersed in octane and MAI was dissolved in DMF. After mixing these two solutions vigorously, it was kept still until two phases of octane and DMF

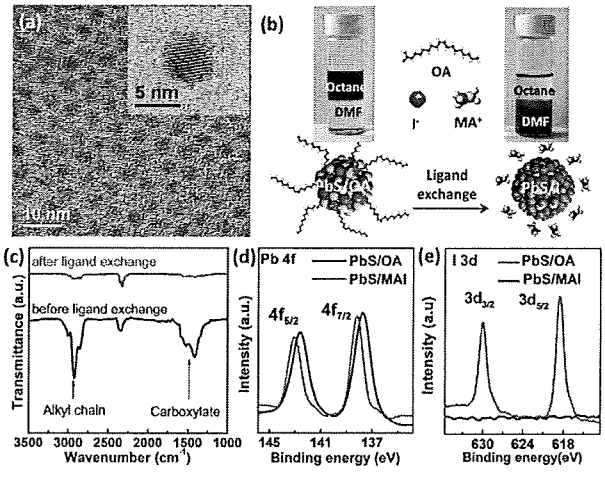

Fig. 1 (a) TEM and HRTEM (inset) image of as-synthesized PbS nanoparticles. (b) Shows the ligand exchange process and the corresponding pictures before and after ligand exchange treatment, respectively. PbS nanoparticles capped with OA ligands were originally dispersed in octane and were transferred into DMF after ligand exchange treatment with MAI molecules. (c) Corresponding FTIR spectra revealing removal of OA ligands on the surface of PbS nanoparticle; XPS spectra of (d) Pb 4f and (e) I 3d revealed the attachment of MAI molecules on PbS nanoparticles.

Published on 11 January 2016. Downloaded by National Chiao Tung University on 30/05/2016 03:34:40.

became well-separated. As shown in Fig. 1(b), the original mixed dispersion containing PbS nanoparticles with OA ligands in octane (top phase) turned clear, whereas the DMF solution (bottom phase) turned dark brown after the ligand-exchange treatment because of the precipitation of the MAI-capped PbS nanoparticles. The detailed synthesis of PbS nanoparticles and the ligand-exchange treatment are described in the ESI.† The surface properties of the PbS nanoparticles were analyzed through Fourier transform infrared spectroscopy (FTIR) and X-ray photoelectron spectroscopy (XPS). Fig. 1(c) depicts the FTIR transmission spectra of PbS nanoparticles before and after the ligand-exchange treatment. The bands at 2930 cm^{-1} and 2850 cm^{-1} are assigned to antisymmetric and symmetric C–H stretching vibrations of the $-CH_2-$ groups in the hydrocarbon moiety of the long alkyl chain, respectively, and those at 1525 cm^{-1} and 1420 cm^{-1} are associated with the COO– vibration modes in the OA molecules.[21,22,25] Following the ligand-exchange treatment, the absorption intensities of the characteristic COO– bands and the $-CH_2-$ vibrational bands decreased substantially, indicating that a large amount of the OA ligands were removed. The XPS results further confirmed the formation of the precursor (MAI)-capped PbS nanoparticles following the ligand-exchange treatment as shown in Fig. 1(d) and (e). The formation of Pb–I bonds increased the Pb $4f_{5/2}$ and $4f_{7/2}$ binding energies because the Pb–I bonds between Pb and MAI molecules have a higher binding energy than the Pb–O bonds between Pb and OA molecules.[22,26] Moreover, the iodine-binding energies of I $3d_{5/2}$ and $3d_{3/2}$ matched well with those of iodine in the bulk of PbI_2,[27] further confirming the attachment of the iodine ligands to the PbS nanoparticles. It is noted that after ligand exchange treatment with MAI molecules, the iodide anions were bound to the lead atoms on the PbS surface and surrounded with MA^+ ($CH_3NH_3^+$) cations as shown schematically in Fig. 1(b).[22] These MAI-capped PbS nanoparticles could be homogeneously dispersed in DMF and were fully compatible with the perovskite precursor for device fabrication.

After the ligand-exchange treatment, the MAI-capped PbS nanoparticles were intermixed with the pristine perovskite precursor solution (MAI and $PbCl_2$) for device fabrication. First, MAI-capped PbS nanoparticles dispersed in DMF were added into the perovskite precursor solution, consisting of 0.5, 1.0, and 1.5 wt% MAI-capped PbS nanoparticles (with respect to the total weight of perovskite precursors and PbS nanoparticles). After gently stirring the mixed solution of the perovskite precursor and MAI-capped PbS nanoparticles, the perovskite thin films were deposited on the substrate using spin coating during which the DMF solvent was evaporated in the initial stage. Because the excess organic solvent remaining entrapped in the film may retard the crystallization of $CH_3NH_3PbI_{3-x}Cl_x$,[28] thermal annealing at elevated temperature of 110 °C for 90 min was then applied to drive out the excess organic component for proceeding the crystallization to a perovskite structure. The parameters for preparing the precursor solutions are detailed in the ESI.† The optical absorption spectra of these thin films deposited with and without the addition of MAI-capped PbS nanoparticles were nearly identical (see ESI,† for details), suggesting that the light harvesting of the small amount of PbS nanoparticles is trivial. Nevertheless, the incorporation of these nanoparticles showed substantial morphological and crystalline improvements in the perovskite thin films. Fig. 2(a)–(d) present the evolution of the top-view scanning electron microscopy (SEM) morphology images of the pristine perovskite sample and the samples consisting of 0.5, 1.0 and 1.5 wt% of MAI-capped PbS nanoparticles, respectively. The pristine perovskite sample contained some pinholes and voids, whereas the samples prepared by adding a small amount of MAI-capped PbS nanoparticles (0.5 and 1.0 wt%) in the perovskite solution demonstrated substantial morphological improvements in terms of surface coverage and uniformity of the perovskite films. The improved morphology of perovskite films by intermixing MAI-capped PbS nanoparticles in the precursors can be further supported from the X-ray diffraction (XRD) spectra as shown in Fig. 2(e), where the strong reflections at 14.2° and 28.5° are assigned to the (110) and (220) reflections of the tetragonal perovskite lattice; these reflections became increasingly intense in the thin films deposited with the addition of 0.5 and 1.0 wt% MAI-capped PbS nanoparticles. The perovskite film deposited with 1.0 wt% MAI-capped PbS nanoparticles exhibited the best morphology and crystallinity, consisting of the largest crystal domains of 2–5 μm with reduced domain boundaries and more uniform coverage. The increased integrity of the surface morphology together with the reduced (110) peak widths (*cf.* the fitted peak widths in the ESI†) suggested that introducing a small amount of MAI-capped PbS nanoparticles in the perovskite precursor solution, which could modify the nucleation and growth during perovskite crystallization, substantially improved both the surface morphology and crystallinity of the resulting perovskite films. Adding 1.5 wt% MAI-coated PbS nanoparticles rendered the film morphology discrete with a decreased number of crystals; as the (110) peak decreased significantly in intensity but maintained a peak width comparable to that of the optimal 1.0 wt% sample, as illustrated in the XRD spectra (Fig. 2).

The corresponding photovoltaic performances of devices based on these perovskite films, consisting of a device structure of FTO/compact TiO_2/$CH_3NH_3PbI_{3-x}Cl_x$/spiro-OMeTAD/Au, exhibited a consistent trend with the observation of improved morphology and crystallinity. Fig. 3(a) shows the current density–voltage (J–V) curves of the champion device performances of the perovskite solar cells fabricated using the perovskite precursor solutions with and without the inclusion of MAI-capped PbS nanoparticles under standard simulated solar radiation (AM 1.5, 100 mW cm^{-2}). The detailed parameters of photovoltaic performances are given in Table 1. The pristine perovskite solar cell exhibited a PCE of 14.11%, with an open circuit voltage (V_{oc}) of 0.99 V, a short circuit current density (J_{sc}) of 21.01 mA cm^{-2}, and a FF of 0.68. Device performance was improved when 0.5 wt% of MAI-capped PbS nanoparticles were incorporated in the growth of the perovskite thin film, showing a PCE of 15.10%, a V_{oc} of 0.99 V, a J_{sc} of 20.90 mA cm^{-2}, and an FF of 0.73. The solar cell device fabricated using the perovskite thin film deposited with 1.0 wt% MAI-capped PbS nanoparticles demonstrated a PCE of 17.40%, the highest among the fabricated devices,

 This journal is © The Royal Society of Chemistry 2016

Published on 11 January 2016. Downloaded by National Chiao Tung University on 30/05/2016 03:34:40.

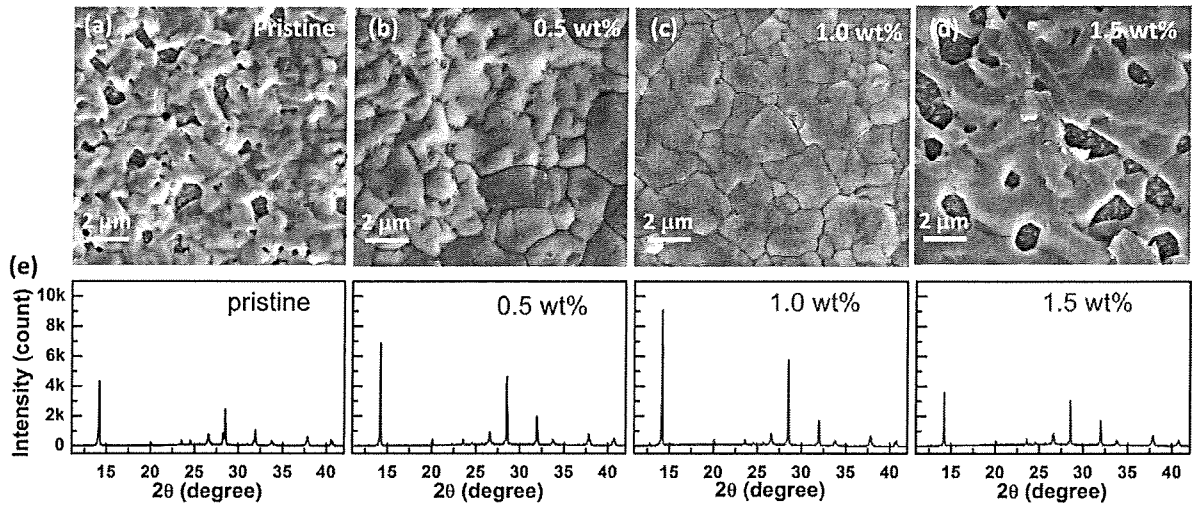

Fig. 2 (a–d) Planar SEM images of $CH_3NH_3PbI_{3-x}Cl_x$ thin films without and with the inclusion of the indicated concentrations of PbS nanoparticles. (e) Corresponding XRD spectra, with (110) peak widths (FWHM) 0.0895°, 0.0752°, 0.0686° and 0.0702°, respectively.

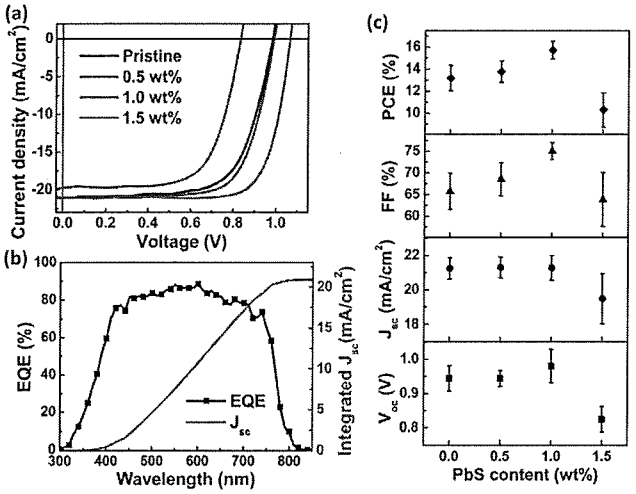

Fig. 3 (a) *J–V* performance corresponded to the champion devices without and with the inclusion of the indicated concentrations of PbS nanoparticles. (b) EQE spectrum and integrated J_{sc} profile of the best performing perovskite solar cell (1.0 wt% PbS nanoparticles). (c) Performance statistics of more than 20 cells for each type of perovskite solar cell.

Table 1 Best and averaged photovoltaic performances of the devices with and without the presence of PbS nanoparticles

Device	V_{oc} (V)	J_{sc} (mA cm^{-2})	FF	PCE_{best} (%)	PCE_{avg}(%)
Pristine	0.99	21.01	0.68	14.11	13.21 ± 1.14
+0.5 wt% PbS	0.99	20.90	0.73	15.10	13.78 ± 0.96
+1.0 wt% PbS	1.07	21.12	0.77	17.40	15.71 ± 0.80
+1.5 wt% PbS	0.84	19.60	0.68	11.25	10.32 ± 1.56

with a V_{oc} of 1.07 V, a J_{sc} of 21.12 mA cm^{-2}, and an FF of 0.77. The external quantum efficiencies (EQE) of this device exhibited a high photon-to-electron conversion efficiency of >80% at 400–750 nm (Fig. 3(b)). The calculated J_{sc} by integrating the full EQE spectrum (20.93 mA cm^{-2}) showed a good agreement with the J_{sc} measured using the solar cell device under standard simulated solar radiation (AM 1.5). Both the EQE and optical absorption spectra (see ESI†) revealed no contribution beyond the absorption edge of the perovskite film, indicating that the small amount of PbS nanoparticles incorporated in the perovskite thin film did not contribute to the additional light harvesting for the enhanced PCEs of devices. As more than 20 cells for each type of perovskite solar cells were fabricated and measured (Fig. 3(c)), it was clearly demonstrated that similar J_{sc} values of these devices were observed, whereas the enhanced PCEs were mainly resulting from the increased FFs after incorporating MAI-capped PbS nanoparticles (both 0.5 and 1.0 wt%). In particular, solar cells fabricated using the perovskite thin films containing 1.0 wt% MAI-capped PbS nanoparticles demonstrated the excellent reproducibility of high FFs, suggesting that substantially improved carrier transport and collection efficiencies of devices were achieved. It is noted that the addition of the MAI-capped PbS nanoparticles may slightly increase the MAI content in the perovskite precursor and therefore, a controlled device prepared using the same amount of excess pristine MAI molecules (no PbS nanoparticles) identical to that of the 1.0 wt% device was also fabricated for comparison. The resultant morphology and device performance were nearly identical to those of the pristine perovskite solar cell (ESI,† Fig. S4), excluding the contribution of excess MAI molecules on the improved morphology and PCEs.

Here, we propose a possible mechanism to account for the effect of the incorporation of the small amount of MAI-capped PbS nanoparticles on the improved morphology and enhanced PCEs of the perovskite solar cell devices. Formation of tetragonal perovskite unit cells requires $CH_3NH_3^+$ organic cations residing at the eight corners with a Pb^{2+} cation at the body center surrounded by six halide anions in an octahedral complex. By sharing the corner halide anion to other octahedra, lead-halide octahedral complexes can form the 3-dimensional (3-D) inorganic framework

Published on 11 January 2016. Downloaded by National Chiao Tung University on 30/05/2016 03:34:40.

of organic–inorganic hybrid $CH_3NH_3PbI_{3-x}Cl_x$.[29] Typically, the ordering or crystallization proceeds efficiently at the interfaces between the perovskite precursors and the TiO_2 compact layer because of the lower nucleation energy barrier at the heterogeneous interfaces.[7,8] For pristine perovskite samples, the nucleation sites of $CH_3NH_3PbI_{3-x}Cl_x$ were mostly restricted on the flat TiO_2 surface, and the subsequent growth of the perovskite crystals to form a framework by interconnecting the octahedrons was largely confined to a limited space at each nucleation site, resulting in small grain-sized perovskite crystals as shown schematically in Fig. 4(a). Some pinholes and voids were observed in pristine perovskite films, possibly because of the fast solvent evaporation rate that hindered the perovskite nucleation on the TiO_2 surface.[10] Recently, a study also reported that the crystallinity and morphology of perovskite thin films were manipulated by adding 1,8-diiodooctane molecules (DIO) as an additive in the perovskite precursor solution, where multiple iodine atoms on DIO molecules lowered the energy barrier to form lead–halide octahedron structures through bidentate chelation, leading to improved coverage and crystallinity of perovskite thin films.[17] In the present work, the surface of MAI-capped PbS nanoparticles was covered with concentrated iodine molecules following the ligand-exchange treatment. It is expected that the MAI-capped PbS nanoparticles may not only improve the miscibility with the perovskite precursor in DMF but also function as effective sites to facilitate the formation of lead–halide octahedrons near the surface of the PbS nanoparticles as illustrated in Fig. 4(b). The MAI-capped PbS nanoparticles that are well dispersed in the perovskite precursors may therefore be considered effective heterogeneous nucleation sites over the entire film, which may also inevitably suppress the number of nucleation sites near the TiO_2 surface, resulting in the growth of larger crystalline domains as illustrated in Fig. 4(b). Thus, the intermixing-seeded growth technique by incorporating a small amount of MAI-capped PbS nanoparticles during film growth may substantially improve the morphology of perovskite films containing larger crystal domains, with a more continuous and uniform surface coverage and enhanced crystallinity.

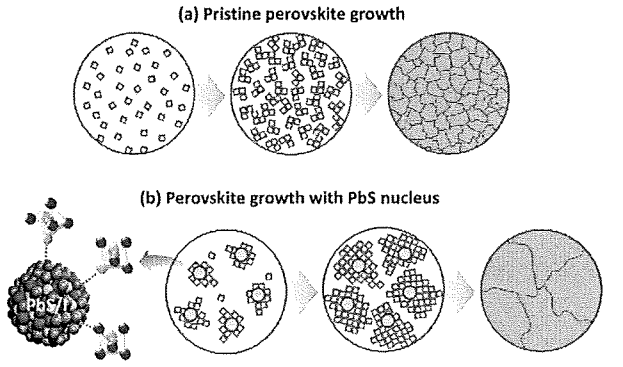

Fig. 4 Proposed nucleation and growth routes of perovskite crystal thin films (a) without and (b) with MAI-capped PbS nanoparticles; the assisted formation of lead–halide octahedrons in the vicinity of an MAI-capped PbS nanoparticle.

In particular, the substantial improvement in the FFs of devices suggested that the efficiency of carrier transport along the direction perpendicular to the substrate of the devices can be increased using the intermixing-seeded growth technique. To gain more insight into the correlation between improved morphology and enhanced PCEs of the perovskite solar cell devices, synchrotron-based grazing incidence wide-angle X-ray scattering (GIWAXS) was performed.[30] Fig. 5(a) and (b) exhibit the 2-dimensional (2D) GIWAXS patterns of the perovskite films without and with the addition of MAI-capped PbS nanoparticles (1.0 wt%). The strong ring patterns in both films indicated the predominantly polycrystalline structure of the perovskite thin films. However, the perovskite thin film deposited with 1.0 wt% MAI-capped PbS nanoparticles exhibited an enhanced (110) and (220) reflections of the $CH_3NH_3PbI_{3-x}Cl_x$ perovskite structure at $q \approx 10$ nm^{-1} and 20 nm^{-1} along the out-of-plane direction (q_z) than that along the in-plane direction (q_y), where q_z and q_y are the respective components of the wave vector, $q = 4\pi\lambda^{-1}\sin\theta$, defined by λ and the scattering angle 2θ. By contrast, the (110) reflection of the pristine sample was of much less preferred orientation as shown in the relative intensity distributions of the (110) reflection as a function of the azimuthal angle φ in Fig. 5(c), which were extracted from the pole figures transformed from the corresponding 2D GIWAXS patterns. In particular, the deduced (110) intensity in the vertical direction ($\varphi = 90° \pm 10°$) for the sample deposited with 1.0 wt% MAI-capped PbS nanoparticles was approximately twofold higher than that for the pristine sample. Because there is a missing wedge angle of ±3.4° in the vicinity of the vertical direction of the pole figures (ESI†),[31,32] the intensities based on the GIWAXS data could only be compared

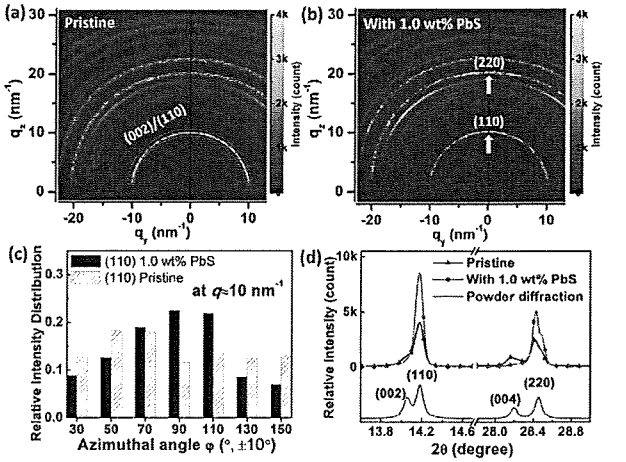

Fig. 5 GIWAXS patterns for the perovskite thin films formed (a) without and (b) with the inclusion of 1.0 wt% of MAI-capped PbS nanoparticles. The vertically preferred [110] reflections are marked. (c) The corresponding relative intensity distributions of (110) reflection as a function of the azimuthal angle, obtained from the pole figures transformed from the 2D GIWAXS patterns in (a) and (b). (d) XRD data (measured with λ = 1.5406 Å) for the characteristic [002] and [110] reflections of two perovskite films without and with 1.0% MAI-capped PbS nanoparticles as indicated. For comparison of the crystal orientation, a simulated XRD powder profile for randomly oriented perovskite crystals is also shown for the intensity ratio of (002) and (110).

This journal is © The Royal Society of Chemistry 2016

Published on 11 January 2016. Downloaded by National Chiao Tung University on 30/05/2016 03:34:40.

qualitatively along the vertical direction. We further analyzed the XRD spectra of these films from the θ–2θ scan data of Fig. 2(a) and (c) to obtain the quantitative comparison in the vicinity of the vertical direction. By scrutinizing the (110) and (220) reflections of the XRD data (Fig. 5(d)), we discovered that an approximately twofold enhancement of both the (110)/(220) reflections of the perovskite crystals for the sample with the inclusion of 1.0 wt% of MAI-capped PbS nanoparticles compared with those of the pristine sample, accompanied by the simultaneous suppression of neighboring (002)/(004) reflections. The intensity ratios obtained from the XRD results were largely consistent with those obtained from the GIWAXS data. These results suggested that the perovskite film grown using the intermixing-seeded growth technique with the inclusion of MAI-capped PbS nanoparticles could assist both crystal growth and orientation, with the enhanced [110] facet normal preferentially along the direction perpendicular to the substrate of the film, which is parallel to the transport direction of the photo-generated carriers toward the electrodes. Nevertheless, the detailed mechanism of promoting the formation of the (110) preferential crystal orientation along the direction perpendicular to the substrate of the perovskite film by incorporating MAI-coated PbS nanoparticles remains unclear; the clarification of the proposed mechanism requires further investigation on the growth kinetics through synchrotron-based GIWAXS.

Furthermore, we estimated the diffusion lengths of the photo-generated electrons and holes to correlate the relationship between the improved crystallinity and enhanced carrier transport efficiency along the direction perpendicular to the substrate. The measurement of diffusion lengths of photo-generated electrons and holes in perovskite films has been reported in previous studies.[5,6] Briefly, the intrinsic radiative recombination lifetime of the perovskite films based on a diffusion model was used to fit the time-resolved photoluminescence (TRPL) decay curves of the perovskite films, where a certain type of photo-generated carrier (electron or hole) is transferred to determine the carrier diffusion properties. The fitting equation was derived from the 1-dimensional diffusion model of a semiconductor[5,6,33–37] and the details of the one-dimensional diffusion model and fitting equations were described in the ESI.† The diffusion lengths of both photo-generated holes and electrons can be individually determined by using different quenching materials. As shown in Fig. 6(a), the quenching layers consisting of an electron acceptor PCBM and a hole acceptor spiro-OMeTAD were deposited atop the $CH_3NH_3PbI_{3-x}Cl_x$ thin film to obtain diffusion coefficients and diffusion lengths of the electrons and holes, respectively. Photoluminescence (PL) intensities for both pristine and 1.0 wt% MAI-capped PbS-incorporated perovskite thin films were substantially quenched because the radiative recombination processes were strongly suppressed due to the additional charge transfer channel from the perovskite thin films to the carrier-quenching materials (Fig. 6(b)). The inclusion of quenching layers substantially facilitated the PL decay efficiencies and reduced the decay lifetime compared with the neat $CH_3NH_3PbI_{3-x}Cl_x$ thin film (without quenching layer) as shown in Fig. 6(c) and 6(d). The neat pristine $CH_3NH_3PbI_{3-x}Cl_x$ thin film exhibited a

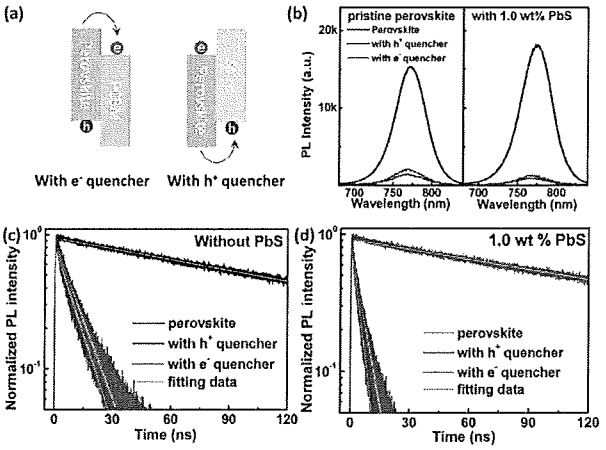

Fig. 6 (a) PCBM and spiro-OMeTAD were deposited on perovskite thin films for quenching photo-generated electrons and holes, respectively. The corresponding PL spectra (measured with and without the quenching layer) of the pristine perovskite and the perovskite with 1.0 wt% of PbS nanoparticle are shown in (b). (c) and (d) respectively presented the corresponding TRPL decay profiles measured with and without the quenching layer.

lifetime τ of 160.72 ns, whereas the PL decay lifetime decreased to τ_e = 8.23 ns and τ_h = 11.81 ns when in contact with electron- and hole-quenching materials, respectively. For the perovskite $CH_3NH_3PbI_{3-x}Cl_x$ thin film with the inclusion of 1.0 wt% of MAI-capped PbS nanoparticles, the PL intensity is enhanced as a result of improved crystallinity of the film and the PL lifetime for the neat film without a quenching layer was 176.39 ns, slightly longer than that of the pristine sample. However, the corresponding PL decay lifetime of the sample with the presence of an electron- and a hole-quenching layer were shortened to a large fraction with τ_e = 3.53 ns and τ_h = 5.17 ns, respectively, indicating that more efficient charge transfer occurred. Table 2 lists the resulting diffusion lengths of the photo-generated electrons and holes obtained using the fitting equation of the diffusion model. Both electrons and holes exhibited long diffusion lengths >1 μm, consistent with previously reported result of the $CH_3NH_3PbI_{3-x}Cl_x$ thin films.[5,6] The enhanced diffusion lengths of 1405 nm for electrons and 1329 nm for holes in the sample with the inclusion of 1.0 wt% MAI-capped PbS nanoparticles were observed, compared with the values of 1192 nm for electrons and 1142 nm for holes of the pristine $CH_3NH_3PbI_{3-x}Cl_x$ sample. Because the transport dynamics of these photo-generated carriers in perovskite materials are sensitive to charge traps and defect states, the enhanced carrier

Table 2 Electron and hole diffusion length derived from TRPL measurement

Sample	τ (ns)	τ_e (ns)	τ_h (ns)	Electron diffusion length[a] (nm)	Hole diffusion length[a] (nm)
Pristine perovskite	160.72	8.23	11.81	1192 ± 72	1142 ± 92
With 1.0 wt% PbS	176.39	3.53	5.17	1405 ± 67	1329 ± 101

[a] Variation of the diffusion length was derived from the fitting errors.

Published on 11 January 2016. Downloaded by National Chiao Tung University on 30/05/2016 03:34:40.

diffusion lengths of both electrons and holes indicated more efficient carrier transport along the film, showing a good consistency with the enhanced crystallinity observed along the direction perpendicular to the substrate. These results may account for the largely enhanced FFs and PCEs of perovskite solar cell devices deposited through the unique intermixing-seeded growth technique with the incorporation of MAI-capped PbS nanoparticles during film growth.

Conclusions

In conclusion, we demonstrated a novel intermixing-seeded growth technique to obtain high-performance planar heterojunction perovskite solar cells. Through interfacial engineering with ligand-exchange treatment, a small amount of MAI-capped PbS nanoparticles intermixed with the perovskite precursor solution functioned as effective heterogeneous nucleation sites to promote the formation of the inorganic framework of perovskite lattice structures, substantially improving the morphology and PCEs of the planar heterojunction perovskite solar cells. In particular, enhanced crystallization and more efficient carrier transport along the direction perpendicular to the substrate of the devices were realized using the proposed technique. It is expected that performances of the planar heterojunction perovskite solar cells fabricated through this novel approach can be further improved through rational design of nanoparticles and surface ligands.

Author contribution

Shao-Sian Li designed the materials and experiments and wrote the manuscript; Chi-Huang Chang and Chung-Wei Lin fabricated the solar cells and carried out the electrical measurements; Ying-Chiao Wang and Di-Yan Wang carried out material characterization; Jou-Chun Lin synthesized PbS nanoparticles; Hwo-Shuenn Sheu, Hao-Chung Chia, Wei-Ru Wu and U-Ser Jeng carried out the synchrotron-based 2D GIWAXS measurements and resolved the lattice structure by Rietveld refinement of XRD data; Raman Sankar, Fang-Cheng Chou, Chia-Chun Chen and Chi-Te Liang helped the discussion of material and device characterization; Chun-Wei Chen also wrote the manuscript and supervised the progress of this project.

Acknowledgements

This work is supported by Minster of Science and Technology (MOST), Taiwan (Project No. 103-2119-M-002-021-MY3 and 102-2119-M-002-005) and Taiwan Consortium of Emergent Crystalline Materials (TCECM).

References

1 C. Wehrenfennig, M. Liu, H. J. Snaith, M. B. Johnston and L. M. Herz, *J. Phys. Chem. Lett.*, 2014, **5**, 1300–1306.
2 S. Sun, T. Salim, N. Mathews, M. Duchamp, C. Boothroyd, G. Xing, T. C. Sum and Y. M. Lam, *Energy Environ. Sci.*, 2014, **7**, 399–407.
3 M. A. Green, A. Ho-Baillie and H. J. Snaith, *Nat. Photonics*, 2014, **8**, 506–514.
4 Q. Lin, A. Armin, R. C. R. Nagiri, P. L. Burn and P. Meredith, *Nat. Photonics*, 2014, **9**, 106–112.
5 G. Xing, N. Mathews, S. Sun, S. S. Lim, Y. M. Lam, M. Gratzel, S. Mhaisalkar and T. C. Sum, *Science*, 2013, **342**, 344–347.
6 S. D. Stranks, G. E. Eperon, G. Grancini, C. Menelaou, M. J. Alcocer, T. Leijtens, L. M. Herz, A. Petrozza and H. J. Snaith, *Science*, 2013, **342**, 341–344.
7 T. A. Berhe, W.-N. Su, C.-H. Chen, C.-J. Pan, J.-H. Cheng, H.-M. Chen, M.-C. Tsai, L.-Y. Chen, A. A. Dubale and B.-J. Hwang, *Energy Environ. Sci.*, 2016, DOI: 10.1039/C5EE02733K.
8 J. W. Gibbs, *Am. J. Sci.*, 1878, 441–458.
9 M. Saliba, K. W. Tan, H. Sai, D. T. Moore, T. Scott, W. Zhang, L. A. Estroff, U. Wiesner and H. J. Snaith, *J. Phys. Chem. C*, 2014, **118**, 17171–17177.
10 G. E. Eperon, V. M. Burlakov, P. Docampo, A. Goriely and H. J. Snaith, *Adv. Funct. Mater.*, 2014, **24**, 151–157.
11 H.-L. Hsu, C.-P. Chen, J.-Y. Chang, Y.-Y. Yu and Y.-K. Shen, *Nanoscale*, 2014, **6**, 10281–10288.
12 Y. Wu, A. Islam, X. Yang, C. Qin, J. Liu, K. Zhang, W. Peng and L. Han, *Energy Environ. Sci.*, 2014, **7**, 2934–2938.
13 N. J. Jeon, J. H. Noh, Y. C. Kim, W. S. Yang, S. Ryu and S. I. Seok, *Nat. Mater.*, 2014, **13**, 897–903.
14 H. B. Kim, H. Choi, J. Jeong, S. Kim, B. Walker, S. Song and J. Y. Kim, *Nanoscale*, 2014, **6**, 6679–6683.
15 X. Song, W. Wang, P. Sun, W. Ma and Z.-K. Chen, *Appl. Phys. Lett.*, 2015, **106**, 033901.
16 C. Y. Chang, C. Y. Chu, Y. C. Huang, C. W. Huang, S. Y. Chang, C. A. Chen, C. Y. Chao and W. F. Su, *ACS Appl. Mater. Interfaces*, 2015, **7**, 4955–4961.
17 P. W. Liang, C. Y. Liao, C. C. Chueh, F. Zuo, S. T. Williams, X. K. Xin, J. Lin and A. K. Jen, *Adv. Mater.*, 2014, **26**, 3748–3754.
18 C. Zuo and L. Ding, *Nanoscale*, 2014, **6**, 9935–9938.
19 M. A. Hines and G. D. Scholes, *Adv. Mater.*, 2003, **15**, 1844–1849.
20 N. Zhao, T. P. Osedach, L.-Y. Chang, S. M. Geyer, D. Wanger, M. T. Binda, A. C. Arango, M. G. Bawendi and V. Bulovic, *ACS Nano*, 2010, **4**, 3743–3752.
21 Z. Ning, H. Dong, Q. Zhang, O. Voznyy and E. H. Sargent, *ACS Nano*, 2014, **8**, 10321–10327.
22 S. Kim, J. Noh, H. Choi, H. Ha, J. H. Song, H. C. Shim, J. Jang, M. C. Beard and S. Jeong, *J. Phys. Chem. Lett.*, 2014, **5**, 4002–4007.
23 Z. J. Ning, X. W. Gong, R. Comin, G. Walters, F. J. Fan, O. Voznyy, E. Yassitepe, A. Buin, S. Hoogland and E. H. Sargent, *Nature*, 2015, **523**, 324–328.
24 D. N. Dirin, S. Dreyfuss, M. I. Bodnarchuk, G. Nedelcu, P. Papagiorgis, G. Itskos and M. V. Kovalenko, *J. Am. Chem. Soc.*, 2014, **136**, 6550–6553.
25 S.-S. Li, Y.-C. Wang, C.-M. Tsai, C.-Y. Wen, C.-H. Yu, Y.-P. Yang, J.-C. Lin, D.-Y. Wang, C.-C. Chen, Y.-C. Yeh and C.-W. Chen, *Nanoscale*, 2015, **7**, 14532–14537.

 This journal is © The Royal Society of Chemistry 2016

Published on 11 January 2016. Downloaded by National Chiao Tung University on 30/05/2016 03:34:40.

26 J. Y. Woo, J.-H. Ko, J. H. Song, K. Kim, H. Choi, Y.-H. Kim, D. C. Lee and S. Jeong, *J. Am. Chem. Soc.*, 2014, **136**, 8883–8886.
27 W. MingáLau, *J. Mater. Chem.*, 2005, **15**, 4555–4559.
28 W. Zhang, M. Saliba, D. T. Moore, S. K. Pathak, M. T. Horantner, T. Stergiopoulos, S. D. Stranks, G. E. Eperon, J. A. Alexander-Webber, A. Abate, A. Sadhanala, S. Yao, Y. Chen, R. H. Friend, L. A. Estroff, U. Wiesner and H. J. Snaith, *Nat. Commun.*, 2015, **6**, 6142–6151.
29 D. B. Mitzi, *J. Chem. Soc., Dalton Trans.*, 2001, 1–12.
30 U.-S. Jeng, C. H. Su, C.-J. Su, K.-F. Liao, W.-T. Chuang, Y.-H. Lai, J.-W. Chang, Y.-J. Chen, Y.-S. Huang and M.-T. Lee, *J. Appl. Crystallogr.*, 2009, **43**, 110–121.
31 C.-M. Liu, Y.-W. Su, J.-M. Jiang, H.-C. Chen, S.-W. Lin, C.-J. Su, U.-S. Jeng and K.-H. Wei, *J. Mater. Chem. A*, 2014, **2**, 20760–20769.
32 W.-R. Wu, U.-S. Jeng, C.-J. Su, K.-H. Wei, M.-S. Su, M.-Y. Chiu, C.-Y. Chen, W.-B. Su, C.-H. Su and A.-C. Su, *ACS Nano*, 2011, **5**, 6233–6243.
33 A. Haugeneder, M. Neges, C. Kallinger, W. Spirkl, U. Lemmer, J. Feldmann, U. Scherf, E. Harth, A. Gügel and K. Müllen, *Phys. Rev. B: Condens. Matter Mater. Phys.*, 1999, **59**, 15346–15351.
34 R. R. Lunt, J. B. Benziger and S. R. Forrest, *Adv. Mater.*, 2010, **22**, 1233–1236.
35 H. Najafov, B. Lee, Q. Zhou, L. Feldman and V. Podzorov, *Nat. Mater.*, 2010, **9**, 938–943.
36 D. Zhitomirsky, O. Voznyy, S. Hoogland and E. H. Sargent, *ACS Nano*, 2013, **7**, 5282–5290.
37 J. E. Kroeze, T. J. Savenije, M. J. Vermeulen and J. M. Warman, *J. Phys. Chem. B*, 2003, **107**, 7696–7705.